Utrecht University

Graduate School of Life Sciences
MSc Science and Business Management

Quantitative Methods for 3D Human Gastruloids Image Analysis

Examiner: Prof. Dr. Alexander van Oudenaarden
Student Coordinator: Prof. Dr. Jop Kind
Daily Supervisors: Dr. Nune Schelling and Dr. Vincent van Batenburg

Andrea Longo
Student ID: 1355635

Academic year 2021/2022

Table of Contents

Laymen summary

Ethical concerns and technical difficulties limit the study of human embryonic development. The current knowledge on the events occurring within the first weeks of human development is based mainly on samples analyzed around a century ago. Researchers have always been studying mammalian development primarily on murine models or primates, identifying key molecular information that cannot be generalized to all mammalian species. Recently, models derived from human embryonic stem cells have been developed in a dish, opening new opportunities for the field of developmental biology. In fact, these cellular aggregates self-assemble and have features of the *gastrulating* embryo. Gastrulation is a succession of events that enable the establishment of body axes and organogenesis. The models developed are called *gastruloids*. They still need to be further investigated to assess the validity of the surrogate system. For this reason, developmental biologists are designing experiments to characterize them. Experiments conducted include visualization techniques, such as immunofluorescence. This visualization technique is based on the detection of a fluorescent signal coming from a labelled antibody that recognizes a protein of interest. Thanks to the digital images produced at the microscope, it is possible to characterize the spatial organization of cells expressing several genes of interest. The limitation of this technique is that it only allows to descriptively present the results obtained. In this work, we developed a collection of methods to extract *quantitative* information from images of human gastruloids.

Digital images are three-dimensional matrices of single units (pixels) that possess spatial coordinates and intensity information. Employing a *machine learning* algorithm, we processed the images collected. As a result, we identified and labelled all nuclei that expressed two genes involved in early development: FOXA2 and SOX17. To proceed with the quantification, we measured the levels of expression of these two proteins in time. Collecting 23 samples, we demonstrated a dramatic change of FOXA2/SOX17 expression. Next, we quantitatively assessed the elongation of SOX17 single positive cells. Furthermore, we measured the spatial organization of SOX17 nuclei. These nuclei were visually disposed along single file tracks, and our techniques allowed to represent the alignment computationally.

In conclusion, with this project we quantified gene expression dynamics and morphological changes of nuclei expressing genes involved in the early development of the human embryo.

Abstract

The study of early developmental stages in humans was limited by technical difficulties and ethical concerns. As a consequence, the scientific community does not have an experimental system able to generate enough reliable data about **human development**. For this reason, new models need to be developed. Recently, multi lineage organoids were generated *in vitro* to model post-implantation events (~2 weeks post-fertilization). These 3D aggregates derived from human embryonic stem cells are called **gastruloids** because they mimic events of the early stages of gastrulation. Although the visualization of such samples produced informative results, the *qualitative* assessment of events remains a limitation intrinsic to the method. In this work, we describe a workflow useful to extract meaningful *quantitative* information from Z-stacks of human gastruloids. Performing nuclear **segmentation** with *Cellpose*, we identified 144,592 nuclei expressing **FOXA2** and **SOX17**, two transcription factors involved in early development. Processing iteratively single optical sections of 23 gastruloids, we were able to measure markers intensity over time. Furthermore, combining tools in *Fiji* and custom functions in *R*, we recorded nuclear shape changes and cellular alignment events. The pipeline developed allows quantification of features which would have been only described by looking at the images. This study serves as a collection of open access tools for researchers to perform accurate image analysis from 3D digital images.

Abbreviations

CNN: Convolutional Neural Network

EMT: epithelial-to-mesenchymal transition

hESCs: human embryonic stem cells

hPSCs: human pluripotent stem cells

PA: post-aggregation

PASE: post-implantation amniotic sac embryoids

Introduction

Immunofluorescence and hematoxylin & eosin staining are used to visualize gene expression and tissues organization. These techniques became routine experiments in research labs and clinics since decades. The main limitation of these experiments, however, is that the data produced can be analyzed only qualitatively, generating mere descriptive results. For many applications it is sufficient to non-quantitatively assess a specific biological observation (Z. Munn, 2010). In these cases, the goal of imaging experiments is to select downstream experiments to precisely measure the phenomenon of interest. Nonetheless, for a precise characterization of biological processes, it is recommended to generate objective and robust quantitative data (D.L Raunig et al., 2015). Up to now, a powerful method used to quantify gene expression from imaging data is the quantification of single RNA molecule expressed; however, this is still impractical for big tissues and does not directly measure the protein levels. Thanks to the technological advantage and the recent large-scale employment of artificial intelligence systems (A. Valizadeh and M. Shariatee, 2021), the development of automated tools to quantify data from images are gaining traction. Life science companies and academical research groups are developing powerful computational toolboxes to extract informative and quantifiable features from imaging data (A. Alexander, 2019). The ultimate goal is to broaden the research questions that imaging experiments can answer. Progresses in microscope manufacturing and machine learning algorithm will make sure that the goal is achieved, enhancing the resolution of imaging-based experiments.

In this report, we combined a collection of methods useful to quantify results generated with imaging experiments. The pipeline developed is suited for any kind of 3D multicellular sample imaged. We tested it on images of human gastruloids. In this introduction, we provide a summary of recent advantages in **human gastruloids development** and an overview about **methods used to quantify imaging data**.

Gastruloids to visualize human post-implantation events in vitro

The study of human developmental biology is limited by technical difficulties to visualize post-implantation events, occurring when the blastocyst establishes a connection with the uterus, starting **gastrulation**. Additionally, international bioethical laws prohibit the culture of human embryos further than 14 days post-fertilization and limit the experiments that can be done on human embryos generated with in-vitro fertilization techniques (J. Fu et al., 2020). Human embryos start gastrulation around week 2 post-fertilization (S. Ghimire et al., 2021). At this developmental time point, body axes specification and organogenesis occur. The knowledge available derives from studies on mice models and from rare human samples described a century ago by the Carnegie Institute of Washington (S. Ghimire et al., 2021). It is necessary to characterize gene expression dynamics driving cell fate determination during gastrulation, in order to understand cellular processes that induce organogenesis while body axes are established.

Gastrulation initiates with the formation of the primitive streak, enabling the three germ layers formation due to the epithelial-to-mesenchymal transition (**EMT**) of epiblast cells (G.C. Schoenwolf and W.J. Larsen, 2009) (Fig. 1a). The switch from E-Cadherin to N-Cadherin is a marker of EMT (G.L. Radice et al., 1997). In this process, some epiblast cells undergo transcriptional programs that enable the delamination and migration through the primitive streak, finally migrating cranially while generating **ectoderm**[1], **mesoderm**[2] and **definitive endoderm**[3]. In later stages of gastrulation, notochord, somite and neural tube are formed. The gradients of transcription factors and signaling molecules established allows the embryo to develop organs with a precise rostral-caudal and dorsal-lateral disposition. These events, partially resolved in model organisms, need to be elucidated directly in humans to gain insights about physiological development.

On this account, a variety of **in vitro models** of the gastrula have been developed to mimic the cellular processes taking place and to visualize samples. The common feature of the models that have been developed is that they are all based on the manipulation of human pluripotent stem cells (hPSC). These cells, either embryonic or induced, are treated according to different protocols to generate: post-implantation amniotic sac embryoids (PASEs), human epiblast models, 2D gastruloids and 3D gastruloids (S.C. van den Brink and A. van Oudenaarden, 2021).

PASEs advantages consist in the formation of a cavitary structure surrounded by two different epithelia: squamous, on one side, and a columnar, on the other (Y. Shao et al., 2017). Therefore, revealing bipolarity, these models histologically resemble the amniotic ectoderm and the epiblast. However, a limitation of the system consists in the lack of cell expressing markers of the three germ layers. Additional models developed are **human epiblast models**. These aggregates form epithelial sacs that express SOX2, OCT4 and NANOG, pluripotency markers expressed by the epiblast in vivo (Y. Zheng et al., 2021). Structures E-Cadherin positive were reported in the epiblast-like model, however no features of gastrulating embryo have been identified by their gene expression. More complex models, named **2D gastruloids**, are derived using geometrical confinement with micropatterned surfaces. These aggregates showed a spatially organized expression of the three germ layer markers in a hESC culture (Warmflash et al., 2014). hESC colonies, initially expressing the pluripotency markers, start expressing markers of the three germ layers and trophectoderm after pre-treatment (Warmflash et al., 2014, A. Deglincerti et al., 2016, K.T. Minn et al., 2020). Although this system shows gene expression patterns, it lacks of 3D complexity. Recently, promising results were accomplished with **3D gastruloids**, multilineage organoids that grow and self-aggregate forming complex and dynamic structures. 3D gastruloids expressed three germ layer markers: SOX2, BRA and SOX17 (Fig. 1b). Their anteroposterior (AP) gene expression profile revealed spatially

---

[1] Precursor of nervous system, sensory organs and epidermis.
[2] Initially disposed as intermediate layer of cells between the ectoderm and the definitive endoderm, and it is the precursor of heart, kidney, endothelium, muscle and cartilage.
[3] Precursor of gastrointestinal organs.
(Source: LifeMap Discovery: Embryonic Development Database)

organized expression of node- and cardiac mesoderm- associated genes, with similarities to the better characterized mouse gastruloid model (N. Moris et al., 2020). However, this system has major limitations: a low number of replicates can be generated and gastruloids can be cultured up to 4 days. In an independent study, a novel protocol has been established to generate high number of 3D gastruloids, which can grow up to months, and express markers for each germ layer (Fig. 1c). These 3D gastruloids polarized their gene expression forming the meso-endoderm and neural compartment, when breaking symmetry, 4 days post-aggregation. This system showed the presence of cells with transcriptional features of the primitive gut tube. Additional cell types were found, such as neural progenitors, providing the field with a complex 3D model of human development (Z.T. Olmsted and J.L. Paluh, 2021).

The human gastruloid model used in this study (Fig. 1d) are generated from the hESCs reporter line adopted in N. Moris et al., 2020 (Fig. 1b), following a modified version the protocol published by Z.T. Olmsted and J.L. Paluh, 2021 (Fig. 1c). We focused our study on cells expressing **FOXA2** and **SOX17**, respectively endodermal marker and endodermal/endothelial marker (I. Burtscher and H. Lickert, 2009, Y. Nakajima-Takagi et al., 2013, C. Yin, 2017). Whereas SOX17 was expressed in both 3D models described (Fig. 1b-c), FOXA2 was detected only in human gastruloids generated with the Z.T. Olmsted and J.L. Paluh protocol. We focused on these two markers to study early dynamics of developing endoderm and endothelium in human gastruloids.
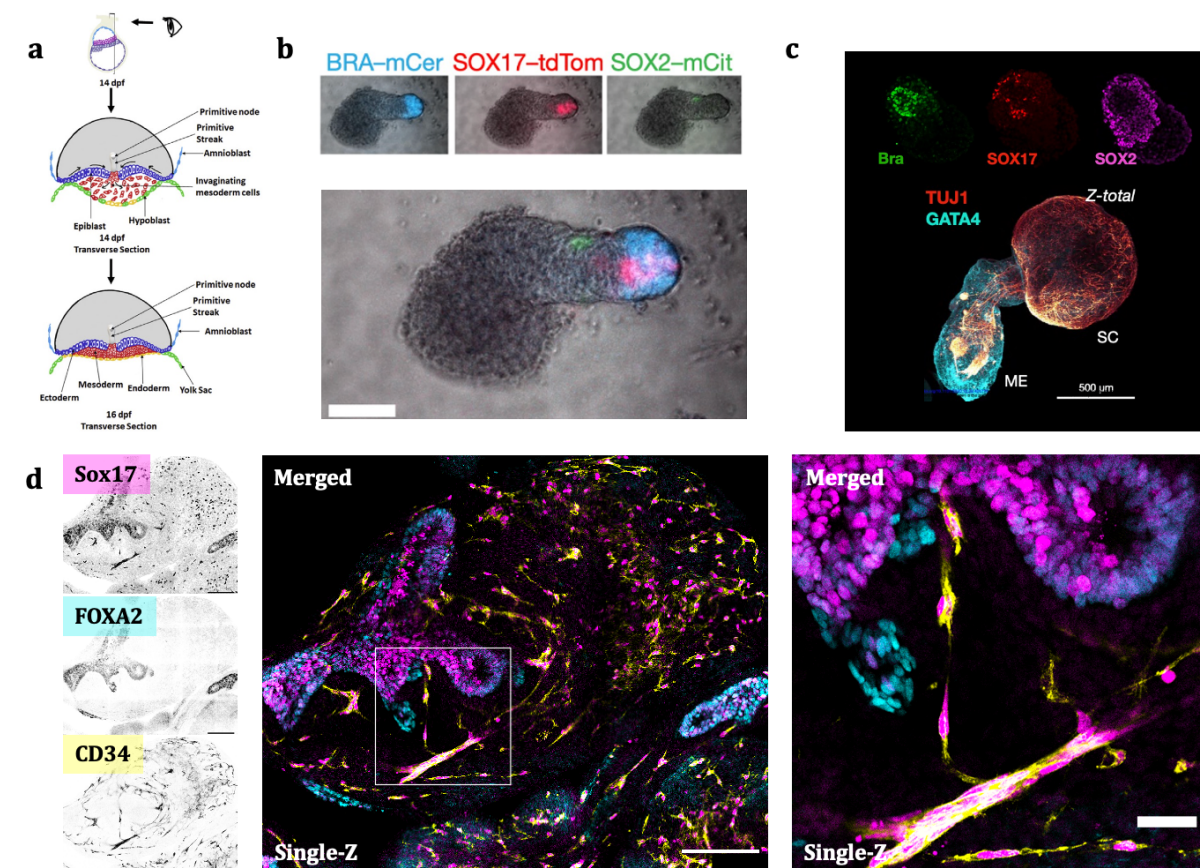
Fig. 1: 3D human gastruloids model post-implantation events in vitro. a) Schematic representation of the three germ layers formation in humans (S. Ghimire et al., 2021). b) Day 3 3D human gastruloid derived from RUES2-GLR (reporter line for three germ layer markers) (N. Moris et al., 2020). Top panel: three germ layer markers are expressed. From left to right: BRA (mesoderm), SOX17 (endoderm/endothelium) and SOX2 (ectoderm). Bottom panel: merge of bright-field with the three channels. Scale bar, 100um. c) Top panel: day 3 hiPSCs derived human gastruloids express three germ layers markers. From left to right: BRA (mesoderm), Sox17 (endoderm) and Sox2 (ectoderm). Bottom panel: day 22 hiPSCs derived gastruloid express TUJ1 (neuronal marker, beta-tubulin) and GATA4 (splanchnic mesoderm marker) (Olmsted and Paluh, 2021). d) Single-Z day 13 RUES2-GLR derived human gastruloids express FOXA2 (endoderm), SOX17 (endoderm/endothelium) and CD34 (endothelial marker). Left panel: three channels shown individually. Central panel: three channels merged. Scale bar, 200um. Right panel: zoom-in. Scale bar, 50um.

Aiming to study cellular populations expressing endodermal markers in human gastruloids, we obtained Z-stacks of the 3D aggregates. Then, we applied a pipeline of quantitative image processing methods. The following section will concisely review available methods widely adopted in the image processing field.

Methods to extract quantitative features from digital images

To extract quantitative features from digital images of human gastruloids, we combined open-source tools that allowed **segmentation**, **features extraction** and **data analysis** of all cell nuclei. We focused on two transcription factors, FOXA2 and SOX17, as they were described in early stages of gastruloid development. Segmentation is a computational task that aims to identify and label different classes of objects (e.g. cell nuclei) present in a digital image. Segmentation is achieved by labelling clusters of pixels that are recognized to belong to an object, creating binary masks. The task consists in converting the image into a matrix in which the original pixel gray values are transformed into a binary range. Binarizing the image allows to distinguish foreground from background. It is also possible to perform multi-class segmentation, clustering objects according to a defined number of classes required to be discriminated. This process is called semantic segmentation because in the foreground, objects are grouped according to their different semantics (A.Valizadeh and M. Shariatee, 2019). The computational strategies for image segmentation are different according to the algorithm adopted. Segmentation is performed with one of the following strategies: thresholding-based, edge-based, region-based, energy-based or neural network-based (K. Jeevitha et al., 2020, S.K. Abdulateef and M.D. Salman, 2021). **Thresholding** relies on clustering pixels by setting thresholds in the image histogram to discriminate different objects. **Edge-based** detection algorithms identify the boundaries of objects applying derivatives of first and second order to spot changes in gray values (e.g. Sobel, Prewitt and Laplacian of Gaussians filters) (S.K. Abdulateef and M.D. Salman, 2021). **Region-based** strategies partition the image and cluster pixels in sub-regions with coherent gray values (K. Jeevitha et al., 2020). The process can be achieved by applying machine learning algorithms such as K-means, which iteratively groups pixels in k classes of objects, starting from randomly selected pixels. **Energy-based** algorithms are sophisticated solutions that use active contours to identify objects in the image by minimizing an energy function. The advantage of this strategy is that while finding global minima in the active contours, the algorithm

distinguishes internal borders of the image, unlike the edge-based detection methods (K. Jeevitha et al., 2020). The four methods illustrated are the most common techniques to achieve segmentation. They are often employed in wider pipelines, in combination with additional filters (e.g. Mean or Gaussian) to pre-process the image and reduce sensitivity to noise. Tools such as Ilastik and CellProfiler allow to employ the algorithms previously illustrated without required coding knowledge. With the Ilastik pixel classification workflow, the user can manually highlight the foreground and background so that the software can automatically proceed with semantic segmentation (S. Berg et al., 2019). In CellProfiler, it is possible to build a customized pipeline, combining pre-processing operations with segmentation methods and feature extraction (K. Soliman, 2015). Moreover, if the user has coding experience, the MATLAB Segmenter toolbox is also recommended to perform similar computations, extending the possibilities of investigation combining easy-to-use toolboxes with built-in functions to process digital images. However, in this study perform we performed segmentation with *Cellpose*, a **neural network-based** algorithm (C. Stringer et al., 2020). These strategies are the state-of-the-art techniques because they employ sequential layers of computational units, the so-called artificial neurons. These layers apply different combination of the previously illustrated filters, e.g. edge-detection, to recognize objects. The network is structured to have an input layer, which represents the data to analyze, multiple hidden layers, where the computations take place, and an output layer that produces the results. Each neuron in the hidden layers performs a computation on the input received and pass the output to the neurons in the following layer. In fully connected neural networks, each neuron represents a mathematical operation connected to individual pixels of a greyscale image. This would make the analysis of images unfeasible computationally. Optimization of fully connected neural networks allowed to build the architecture of Convolutional Neural Networks (**CNN**s), suitable for image processing purpose. CNN architecture differs from traditional neural networks due to the presence of convolutional layers, with defined receptive fields, responsible to analyze iteratively partitions of the image. Unlike fully connected neural networks, in CNNs the computational parameters are grouped in n x n kernels, that recognize specific patterns in the image, such as edges and shapes of objects (H.H. Aghdam and E.J. Heravi, 2017). The resolution of the feature maps increases as the data are processed in *deeper* layers. The kernels are applied to all n x n regions of the input image to search for the pattern of interest. Each convolutional layer passes the transformed version of the image to the following layers, until it reaches the output layer. Cellpose is a CNN, and its architecture is based on the U-net, that combines a contracting and expansive path to increase the accuracy of segmentation in the medical and biological fields (O. Ronneberger et al., 2015).

We employed Cellpose to perform 2D segmentation of nuclei expressing FOXA2 and SOX17 in each Z-plane of human gastruloids images. The algorithm produces binarized masks of all nuclei in the image. We further processed the masks in Fiji to extract morphological features and protein expression levels. Then, the data were prepared in R to apply custom functions aiming to visualize cellular patterns.

Results

Human gastruloids expressing an endogenous SOX17 reporter construct, were whole-mount immunostained with anti-FOXA2 antibodies (Fig. 2a). The samples were imaged at the Leica SP8 confocal microscope to obtain **optical sections** of the 3D aggregates. We observed that gastruloids are rounded at early time points post-aggregation (PA). Their shape changes around day 4 PA, when symmetry breaking occurs. Most cells from day 1 to day 4 PA were either single FOXA2 positive (FOXA2^{+}) or FOXA2^{+}/SOX17^{+}. Gastruloids older than 4 days PA, showed to have an increased number of single SOX17^{+} nuclei appearing. These single SOX17^{+} cells have elongated nuclei and seem to be aligned in a chain-like structure. On the other hand, single FOXA2^{+} cells don't show elongated nuclei. They are contiguous and clustered in a tubular-like structure, which in additional experiments, not described in this study, was demonstrated to be also N-cadherin[+]. The observed tracks of elongated SOX17^{+} nuclei are more frequently found at different depth with respect to the Z-planes where the tubular-like structure is in focus. However, some SOX17 signal was detected also in single FOXA2^{+} nuclei clustered in the tubular-like structure, indicating the presence of double positive nuclei in this region. After day 4 PA, single SOX17^{+} cells express CD34, an endothelial surface marker (G. Lin et al., 1995, M.P. Pusztaszeri et al., 2006, J. Yang et al., 2011, L.E. Sydney et al., 2014), when outside the tubular-like structure (Fig. 1d).

In order to quantitatively document these observations, we formulated several research questions. First of all, our goal was to identify an algorithm that segments all true positive nuclei. In fact, the production of accurate binary masks was fundamental to calculate nuclear gray values and positional information. With the information calculated we could proceed to answer our questions. We assessed whether there are changes of transcription factors expression over time. On this account, we wondered if it was possible to discriminate different cell populations according to their marker genes expression. Then, we aimed to examine nuclear elongation, investigating if it is restricted to certain cell populations and/or specific time points. Next, we evaluated if there are any expression features correlated with the nuclear elongation. Finally, we focused on determining whether cells with elongated nuclei are aligned when spreading along the gastruloids surface.

Segmentation of RUES2-GLR human gastruloids

Aiming to perform nuclear segmentation to identify and label all FOXA2 and SOX17 positive nuclei, we compared different segmentation software. We selected **Cellpose**, a CNN that is already trained and is available in the Google Colab with a GPU for faster computation. To achieve our goal of measuring protein levels and extract cell shape features, we needed to generate binary masks of positive nuclei. Our aim was to maximize true positive cell nuclei identification and minimize false positives retention. We manually evaluated the segmentation accuracy by visually assessing the masks fitted to the nuclei while adjusting the algorithm hyperparameters. We compared the two models

available on Cellpose, nuclear and cytoplasmic. We chose the **cytoplasmic model** instead of the nuclear model because the latter segmented only rounded shaped nuclei, without capturing the elongated ones. We tuned the **flow threshold** = 1, **cell probability** = 0 and **cell diameter** = 45, because these settings enabled the algorithm to further increase true positive inclusion in the analysis (Supplementary Fig. 1). Using these hyperparameters and the cytoplasmic masks, we were able to segment most of the elongated and rounded cell nuclei in the gastruloids images.

Next, to identify the channels that we could use to feed the CNN, the adjusted hyperparameters were applied on DAPI, FOXA2 and SOX17 channels. Using DAPI images, we observed a wrongly annotated nuclear shape, which limited the segmentation accuracy causing low true positive rate (Supplementary Fig. 2). On the other hand, nuclear shapes were faithfully captured when generating masks using either the FOXA2 or SOX17 channel (Fig. 2b). This augmented substantially the number of true positives nuclei, further reducing false positives counts. Therefore, in further analyses, we decided to use the combination of masks generated by processing FOXA2 and SOX17 channels, instead of DAPI.

To measure the pixel intensity for all segmented nuclei, corresponding to the expression levels of SOX17 and FOXA2, we applied the masks obtained from FOXA2 and SOX17 on both channels (Fig. 2c). Some false positive nuclei were still detected. Investigating the reason for this inaccuracy, we discovered that SOX17$^+$ nuclei were frequently overexposed, causing the pixels to be saturated (Fig. 2d-e). We found that when the overexposure was prevailing, the algorithm generated ill shaped masks, or no mask at all. This was due to the algorithm inability to distinguish cell borders of saturated objects.

To overcome the saturation issue, we filtered nuclei according to the percentage of saturated pixels in the region of interest (ROI). The identification of saturated pixels was achieved by subtracting a value of 254 to all pixels of the image. This is because in 8-bit digital images, the gray values range from 0 to 2^8. This leaves all pixel gray values equal to 0 except for the pixels saturated, which will have a value equal to 1. Once this step was achieved, we calculated the **integrated density**, product of area and mean gray values, for all ROIs. We obtained the percentage of pixels saturated for all segmented nuclei by dividing the integrated density by the area of the ROI. The threshold was set to include cells with < 25% pixels saturated, as we identified this cut-off as a solution to minimize false positive counts (Fig. 2f).
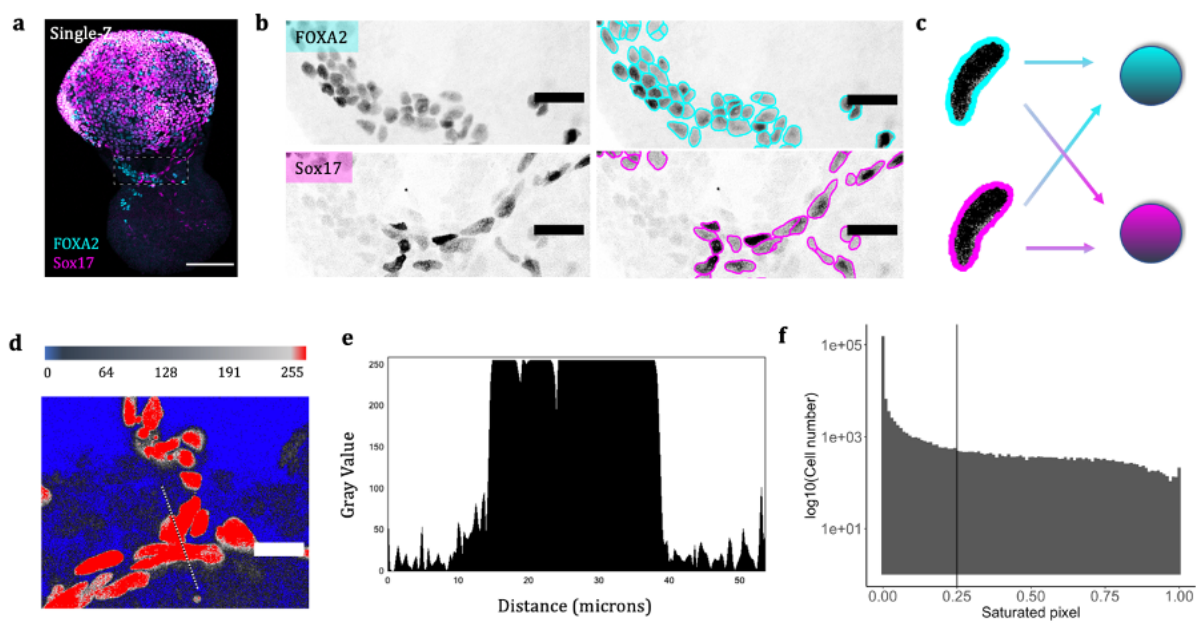
Fig. 2: Segmentation of RUES2-GLR human gastruloids to extract quantitative features at single cell resolution. a) Single-Z of a Day 7 RUES2-GLR human gastruloid expressing FOXA2 and SOX17. Scale bar, 200um. b) Zoom in. On the left, the two channels split, on the right, the cell outlines of segmented cells. Scale bars, 50um. c) All segmented cells have two mean intensity values, one for SOX17 and one for FOXA2, independently from the channel in which they were segmented. d) HiLo LUT applied on single-Z SOX17 channel. Scale bar, 25um. e) Profile plot of the dotted line drawn in Fig. 2d. On the x-axis the length of the line in microns, on the y-axis the signal intensity in R.F.U.. f) Filtering: only cells with < 25% of pixels saturated are retained for the purpose of this study. On the x-axis the percentage of saturated pixels, on the y-axis the $\log_{10}$ transformed cell number; cut-off 0.25.

FOXA2 and SOX17 mean intensity values change in time

Being able to segment cell nuclei with limited inaccuracy we investigated the FOXA2 and SOX17 expression dynamics over time. Therefore, we created a dataset of imaging data from 23 RUES2-GLR human gastruloids expressing these two genes of interest. Two rounds of aggregations and six time points were merged, day 1 (n = 5), day 3 (n = 4), day 4 (n = 5), day 7 (n = 4), day 10 (n = 4) and day 13 (n = 1) (Fig. 3a), to assess possible changes in SOX17 and FOXA2 expression over time. Using Cellpose with adjusted hyperparameters, and applying the filtering strategy previously described, a total total of 144,952 nuclei were segmented for further analysis.

In order to quantify the pixel mean intensity of different subsets of segmented nuclei, we analyzed the combination of FOXA2/SOX17 masks of each gastruloid at all time points. The results were plotted in a scatterplot, showing the mean intensity of SOX17 (x-axis) and the mean intensity of FOXA2 (y-axis) per each time point separately (Fig. 3b). Considering that every dot is a cell, single positive cells are mainly segmented in the respective positive channel, as indicated by the dot color (Fig. 3b). Measuring the ratio between the masks produced from the SOX17 and FOXA2 channels (Fig. 3c), we observed that for all time points, both channels contributed to nuclear segmentation. Although the

ratio between the two masks changes over time, no dramatic variations in masks produced from each channel were reported. Applying two thresholds on mean intensities for both markers, three distinct clusters were defined: single FOXA2$^+$, single SOX17$^+$ and double positives (Fig. 3d).

To analyze the fraction of positive nucleus in time, we visualized each cluster in a normalized bar plot (Fig. 3e). Our results demonstrated differences in FOXA2/SOX17 expression depending on the gastruloids developmental time point. An abundant presence of single FOXA2$^+$ nuclei was detected between day 1 and day 4 PA, when compared to later time points. Analyzing the fraction of positive nuclei in time (Fig. 3e), we found that less than 5% of all segmented nuclei are single SOX17$^+$ at day 1, day 3 and day 4 PA gastruloids, whereas they are 20-50% between day 7 and day 13 PA gastruloids. In contrast, the number of single FOXA2$^+$ nuclei peaked at earlier time points and decreased substantially starting from day 7 PA. Moreover, the number of double positive cells was detected to slowly increase between day 1 and day 10 PA, when compared to the rapid changes in SOX17 and FOXA2 expression. However, the constant increment of double positive cells from day 1 to day 10 PA, was shown to decrease at day 13 PA. Furthermore, at day 13 PA, most cells were either single SOX17$^+$ or double positive, leaving only a small fraction of single FOXA2$^+$ cells. In addition, a high number of double positive cells with saturated mean intensity values in the SOX17 channel (Fig. 3b) were observed to be present. This data indicate that despite the filtering (Fig. 2f), there are still nuclei with a non-negligible saturated SOX17 signal. However, it also indicates that a subset of double positive cells starts expressing SOX17 at higher levels between day 7 and day 10 PA, when compared to double positive nuclei at earlier and later time points. Despite the persistent presence of saturated SOX17 signal, our results suggest that this quantitative method have the resolution required to capture changes in marker gene expression.
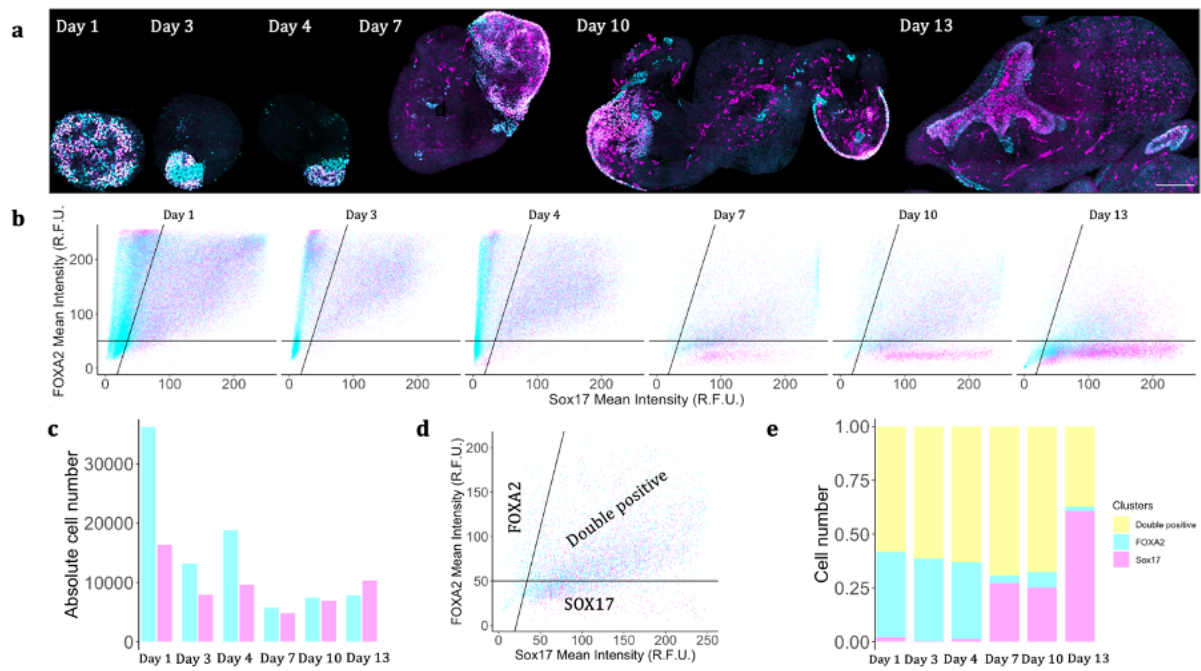
Fig. 3: FOXA2/SOX17 expression dynamics in time. a) RUES2-GLR derived human gastruloid; one example per time point (single Z-planes). FOXA2 in cyan and SOX17 in magenta. Scale bar, 200um. b) Scatterplot where every point is a cell segmented. On the x-axis the mean intensity of SOX17, on the y-axis the mean intensity of FOXA2. The scatterplots are divided according to the gastruloids time points. The color of the dots corresponds to the channel in which each cell has been segmented (magenta for SOX17 and cyan for FOXA2). Lines drawn separate the clusters defined (single FOXA2+, double positive and single SOX17+). c) Bar plot of absolute cell number segmented in FOXA2 (cyan) and SOX17 (magenta) channels at different time points. On the x-axis the time point, on the y-axis the cell number of cells segmented. d) Scatterplot of a day 10 replicate. Three clusters are defined according to the mean intensity of FOXA2 (y-axis) and SOX17 (x-axis). e) Bar plot with fraction of cells at different time points; colors indicate cell clusters (yellow: double positive; cyan: single FOXA2+; magenta: single SOX17+). On the x-axis the different time points, on the y-axis the normalized cell number (total number of cells segmented = 1).

SOX17+ nuclei elongate

Being able to capture changes in gene expression using this quantitative method, we tested the workflow as a tool to evaluate nuclear morphology differences, qualitatively assessed previously. Starting from day 4 PA some single SOX17+ nuclei were observed to have **elongated nuclei**, when compared to single FOXA2+ cells. These elongated single SOX17+ nuclei were observed to be close to each other in space and seemed to be aligned into an organized tracks. Using our quantitative methods, we measured the nuclear aspect ratio of all nuclei belonging to the three clusters defined previously. Aspect ratio is an indicator of an object shape (Fig. 4a), and it is calculated by fitting an ellipse to the object of interest and dividing its major axis by its minor axis (e.g. round objects have aspect ratio equal to 1) (Fig. 4b-c).

We calculated the aspect ratio for all cells segmented and we plotted the distribution of single SOX17+ nuclei (n = 25,723), FOXA2+/SOX17+ nuclei (n = 121,675) and single FOXA2+ nuclei (n = 49,751), aggregating all time points together in a boxplot (Fig. 4d).

14

The plot shows that SOX17 nuclear aspect ratio is significantly higher compared to single FOXA2$^+$ and double positive nuclei (p-value < 2.2x10^{-16}, Mann-Whitney test). The aspect ratio distribution of double positives was significantly higher than single FOXA2$^+$ nuclei (p-value < 2.2x10^{-16}, Mann-Whitney test).

To investigate whether it is possible to understand if the nuclear elongation event, observed in the SOX17 cluster, starts at a specific time point, we analyzed the nuclear aspect ratio of all nuclei, dividing them per time point and cluster (Fig. 4e). SOX17 nuclear aspect ratio slightly increases from day 3 to day 4 PA, and it further increases from day 4 to day 10 PA, with more than 50% of single SOX17$^+$ nuclei having an aspect ratio greater than 1.5. Surprisingly, SOX17 nuclear aspect ratio decreased at day 13. On this account, day 13 PA is the only time point in which a considerably populated subset of single SOX17$^+$ spherical nuclei appear, as most SOX17$^+$ cells were elongated at day 7 and 10 PA gastruloids. On the other hand, single FOXA2$^+$ aspect ratio doesn't show drastic variations, except for the one observed from day 7 to day 13 PA, when the number of single FOXA2$^+$ nuclei was decreased, limiting the robustness of the observation compared to previous time points. Double positive nuclei, instead, followed a trend which is similar to the single SOX17$^+$ nuclei. Indeed, this cluster seems to have nuclear aspect ratio dynamics that are in between the SOX17 and FOXA2 clusters (Fig. 4e).

These results highlight the exclusivity of nuclear elongation for the SOX17 cluster, and partially for the double positive nuclei, from day 3 PA on. However, the methods developed could not identify any specific correlation between the aspect ratio of single SOX17$^+$ nuclei and SOX17 mean intensity (Supplementary Fig. 3).
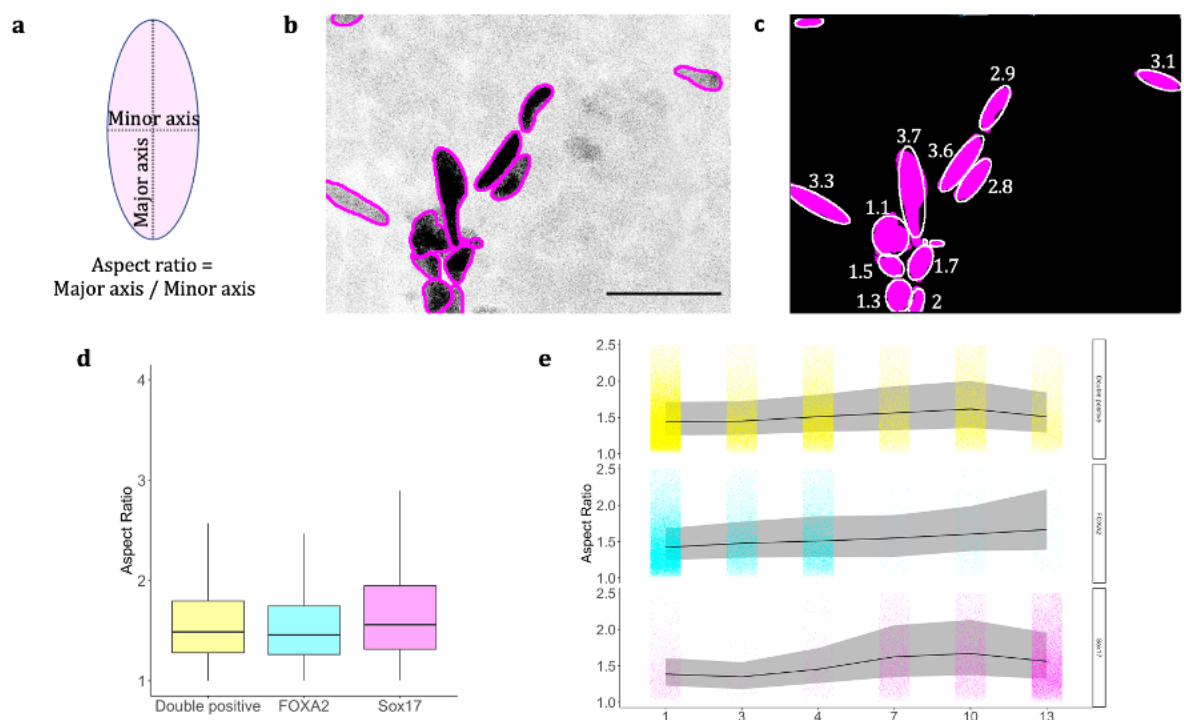

15

Fig. 4: Aspect ratio measurements demonstrate SOX17 nuclear elongation in time. a) Ellipses have two axes: major and minor. Aspect ratio index represents the ratio between the two axes. b) Cell outlines of single SOX17$^+$ nuclei in magenta. Ellipses are fitted to the shapes highlighted in this single-Z image. Scale bar, 50 um. c) Ellipses fitted to single SOX17$^+$ nuclei segmented in Fig. 4b. Aspect ratio of each nucleus is indicated in white. d) Box plot showing the aspect ratio distribution for all clusters. On the x-axis the clusters, on the y-axis the aspect ratio. First and third quartile are shown, as well as the median. e) Line to highlight aspect ratio variations in time for each cluster. On the x-axis the time point, on the y-axis the aspect ratio. Dots represent cells. The line indicates the median. In grey, the interval between the first and third quartile.

Elongated SOX17$^+$ nuclei align

Imaging of gastruloids at different time points highlighted an interesting spatial organization of elongated single SOX17$^+$ nuclei. Elongated FOXA2$^-$/SOX17$^+$/CD34$^+$ nuclei seem to be aligned along a track, whereas rounded FOXA2$^-$/SOX17$^+$/CD34$^+$ appear randomly disposed on the gastruloid surface. To validate the possibility of the existence of a track followed by FOXA2$^-$/SOX17$^+$/CD34$^+$, we examined whether neighbor elongated nuclei have similar orientation in space. We filtered and split single SOX17$^+$ nuclei according to their aspect ratio into two subsets: single SOX17$^+$ nuclei with aspect ratio greater than 1.5 and single SOX17$^+$ nuclei with aspect ratio lower than 1.5 (Fig. 5a).

We measured the **pairwise Euclidean distance** (Fig. 5b), considering the nuclear centroids, and the **pairwise angle difference** between segmented nuclei (Fig. 5c). Nuclear angle difference is measured fitting an ellipse to the object and measuring the angle of the major axis with respect to the x axis of the image. These features are calculated processing individual optical sections, finally aggregating the results of all gastruloid Zs in a single dataset. The procedure is repeated for the two subsets created. Since a considerable number of both rounded and elongated FOXA2$^-$/SOX17$^+$/CD34$^+$ was present only in day 13 PA gastruloid, we decided to apply this method only on this replicate. This decision allowed us to produce a dataset to test (elongated nuclei) and a dataset intended to be a negative control (rounded nuclei).

First, we analyzed the **elongated subset** of FOXA2$^-$/SOX17$^+$/CD34$^+$ nuclei. We created a randomized dataset with authentic distances and random angles (Fig. 5c, dotted ellipses) to assess whether the original observations have a distribution comparable, or not, to a randomized dataset. Using the Euclidean distance and angle difference, two heatmaps were generated. One heatmap includes the authentic distances (x-axis) and authentic angles (y-axis) (Supplementary Fig. 4a), whereas the other displays authentic distances (x-axis) and randomized angle (y-axis) (Supplementary Fig. 4b). Next, we divided the occurrences of each bin of the heatmap obtained from the authentic dataset by the occurrences of each bin of the randomized dataset. Then, to highlight significant exclusivity of events in the authentic dataset, we plotted the $\log_2$ of the ratio between the two heatmaps (Fig. 5d). As a result, we observed that elongated FOXA2$^-$/SOX17$^+$/CD34$^+$ nuclei that are closer in space tend to have a similar angle.

Finally, we generated an additional ratio heatmap for the **rounded subset** of FOXA2⁻/SOX17⁺/CD34⁺ nuclei. As a result, rounded FOXA2⁻/SOX17⁺/CD34⁺ nuclei did not appear to be aligned, because no significant fold increase/decrease was highlighted by the heatmap (Fig. 5d). However, the major limitation of this measurement, is that the angle is computed by fitting an ellipse to the nuclei, which are mostly rounded for this subset. Fitting ellipses to rounded objects is not the optimal strategy to determine an object orientation in space.

These results, however, indicate that the elongated FOXA2⁻/SOX17⁺/CD34⁺ cells surrounding the tubular-like structure (Fig. 5f) are likely to be aligned if they are close in space.
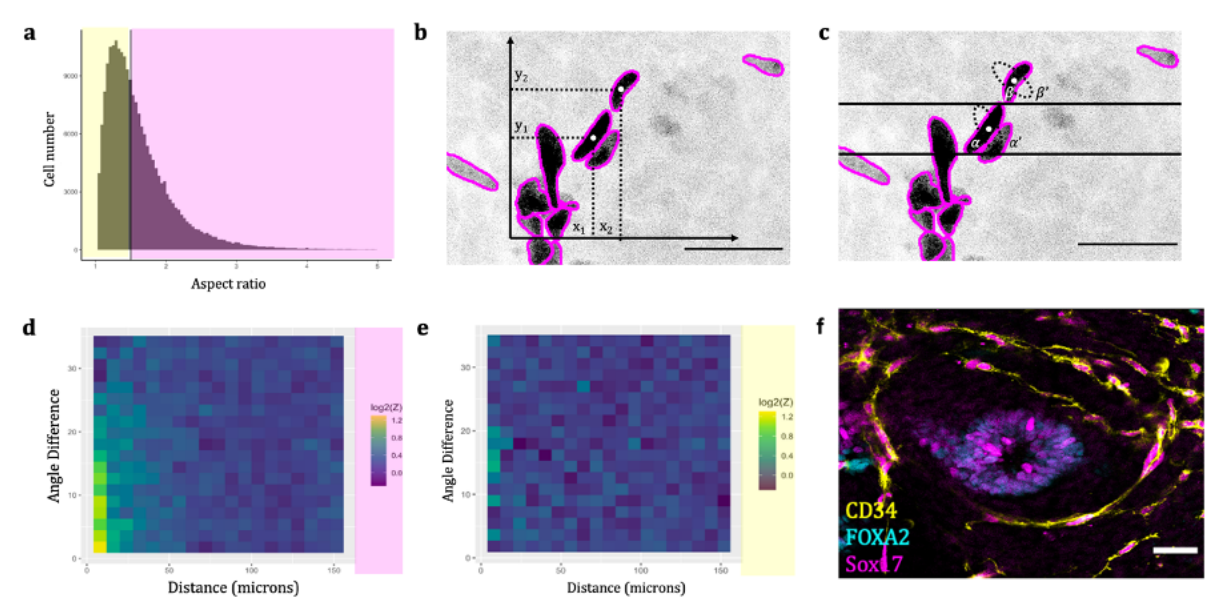
Fig. 5: Elongated SOX17 nuclei align when close in space. a) Histogram showing the aspect ratio distribution of 23 gastruloids SOX17 nuclei (on the x-axis the aspect ratio, on the y-axis the absolute cell number). Elongated cells are shown with a magenta background and rounded cells have a yellow background (cut-off value: 1.5). b) Example of pairwise Euclidean distance calculation. Nuclear centroids in white. The coordinate system used, x- and y- axes, considers the X and Y coordinate of the image itself. Scale bar, 50 um. c) Example of pairwise angle difference calculation. Nuclear centroids in white. A randomized dataset is generated with random angles assigned to each cell (black dotted line indicates the randomization). As the random dataset is generated, the nuclear centroids are fixed, so that the distance does not vary, and the only variable changing is the nuclear angle. Scale bar, 50 um. d) Ratio heatmap of actual observations and randomized dataset for day 13 elongated nuclei (aspect ratio > 1.5). On the x-axis the distance, on the y-axis the angle difference. Colours show the log$_2$ of the ratio between real dataset and randomized. e) Ratio heatmap of actual observations and randomized dataset for day 13 rounded cells (aspect ratio < 1.5). On the x-axis the distance, on the y-axis the angle difference. Colours show the log$_2$ of the ratio between real dataset and randomized. f) Single-Z of day 13 RUES2-GLR human gastruloid. FOXA2, SOX17 and CD34 are shown. Scale bar, 50 um.

Discussion

To recapitulate the results of this study, we established a pipeline of methods useful to quantitatively analyze marker gene expression dynamics, nuclear shape changes and cellular alignment at the single cell resolution in 3D human gastruloids systems.

To start with the computational workflow, we produced 3D images using a confocal microscope. Optical parameters have been inspected in the metadata of the images, and the settings do not change between different imaging sessions. The main limitations of the imaging data obtained are the signal saturation in the SOX17 channel and the bleed-through in the FOXA2 channel. Filtering for cells having less than 25% pixels saturated was determining to avoid the inclusion of ill shaped masks. On the other hand, we did not compensate for the bleed-through detected; however, drawing a diagonal line, we could still define a FOXA2 gate.

The pipeline is then articulated in three main sequential steps: nuclear segmentation, features calculation and data analysis. Using Cellpose, a generalist CNN for 2D cellular segmentation, we selected the hyperparameters that enabled the identification of true positive FOXA2 and SOX17 nuclei in all Z planes of human gastruloids. Once binary masks of true positive nuclei were produced, we measured the mean intensity of the signal coming from both channels; we also calculated their nuclear aspect ratio, Euclidean distance and angle difference. Finally, we organized the dataset to produce plots and heatmaps that allow to visualize the properties of interest.

We demonstrated that *FOXA2 and SOX17 expression changes* within the first two weeks of human gastruloids development. The resolution of the analysis allowed to capture a decreasing number of single FOXA2$^+$ nuclei and an increasing fraction of single SOX17$^+$ nuclei in time. Since all data processed are derived from fixed samples, we cannot infer whether there is a transition between the two clusters or if it is the case of two uncorrelated events. Lineage tracing studies and single cell sequencing or RNA velocity can clarify possible differentiation events involving the cells expressing FOXA2 and SOX17. However, it is still worth to implement this method to perform a preliminary quantitative analysis of genes expressed in 3D model systems. It would be helpful to have a quantitative indication of the expression pattern of genes before proceeding with more sensitive assays. In fact, interpreting the quantitative results generated with our pipeline would help to formulate data driven research questions. In our specific case, however, more replicates should be characterized to produce statistically robust results to claim that the changes in FOXA2 and SOX17 expression are recurrent in human gastruloids. As previously mentioned, the gastruloids processed in this study belong to two independent experiments.

We also showed that we could *measure and compare nuclear aspect ratio* of cells, revealing that single SOX17$^+$ nuclei elongate starting from day 4 PA. The resolution of our methods, however, did not allow to identify any correlation between the aspect ratio of single SOX17$^+$ nuclei and SOX17 mean intensity. The signal intensity of SOX17 was not significantly higher in elongated nuclei when compared to rounded nuclei, or vice versa (Supplementary Fig. 3). For this reason, the level of expression of SOX17 do not appear to be determinant for nuclear elongation.

We also demonstrated *that elongated single SOX17$^+$ nuclei align* while forming connected endothelial cell networks (Fig. 5f). This result is consistent with the observation of motile FOXA2$^-$/SOX17$^+$/CD34$^+$ cells (data not shown) that move and spread in a single file pattern within the gastruloids. We believe that these cells, sensing the environment, create connections with neighbor cells, resulting in organized rod-shaped structures. To prove that these cells move following a specific track, we measured their pairwise distance and angle difference. The angle was estimated by fitting an ellipse to each nucleus to calculate the inclination of the major axis with respect to the x-axis of the image. The major limitation of our method is the negative control employed, which consisted of a dataset of single SOX17$^+$ nuclei with aspect ratio lower than 1.5. In fact, it is not ideal to fit ellipses to rounded objects. Therefore, we cannot be sure about the accuracy of the angle calculated in rounded SOX17$^+$ nuclei. Also rounded FOXA2$^-$/SOX17$^+$/CD34$^+$ cells seem to be connected in a network, but their disposition is not as organized as observed for elongated FOXA2$^-$/SOX17$^+$/CD34$^+$ nuclei (Supplementary Fig. 5).

In conclusion, this works aimed to test a pipeline of methods intended to extract quantitative information from images of 3D multicellular aggregates, such as gastruloids and organoids. The accuracy of the methods developed is directly proportional to the imaging resolution, as it happens for all the machine learning algorithms employed in computer vision. We demonstrated that Cellpose, a simple and ready-to-use CNN for cellular segmentation, performs accurate nuclear identification when processing individual optical sections of human gastruloids. Testing various segmentation methods, such as the MATLAB image segmentation toolbox and CellProfiler, we elected Cellpose as method which maximizes the presence of true positive nuclei and reduce drastically the number of false positives on our imaging data. The methods developed around this segmentation method provide researchers with a powerful quantitative in silico tool. The pipeline is suitable to answer many research questions, ranging from transfection efficiency assessment to imaging-based lineage tracing. In fact, it is easy to imagine the applicability of these methods to quantify the number of cells transfected, or precisely assess the confluency of a cell culture. Additionally, it allows to measure features of cells that migrate in a wound healing assay, also known as scratch assay. Furthermore, in hybridization chain reactions (HCR) experiments, it is essential to create cell masks that allow a precise quantification of labelled single RNA molecules expressed by each cell; for this reason, with the methods illustrated, it would be possible to quantify single RNA molecules within a single nucleus. In addition, the same exact pipeline of methods can be applied on live imaging videos, with the only variation being the introduction of a fourth dimension: time. Finally, since the research is moving fast to develop open-source and straightforward methods for quantitative imaging, we propose to apply this pipeline to perform imaging-based lineage tracing. Various segmentation methods are employed in fate mapping using imaging data (S. Wolf et al., 2022), however Cellpose has not yet been recognized as the gold standard to perform this task. For this reason, it is worth to further optimize the methods described in order to widen their applicability and resoution. In

fact, the pipeline could be optimized by adding a step in which 2D segmentation is transformed in 3D segmentation; to achieve this, it is possible to compute the contours of cell nuclei in focus in different Z-plane, finally aggregating the results in the Z dimension, reconstructing the 3D features of all nuclei. We aim to develop in the future a pipeline on KNIME, a platform which enables to integrate various software developed by multiple stakeholders. This would allow researchers to perform end-to-end data analysis, integrating different software and programming languages, with limited coding knowledge required.

The quantitative image processing pipeline developed has the potential of becoming a straightforward collection of methods to quantify imaging-based results. Considering the fast technological progress, the field of digital imaging will develop systems to reach higher resolution, enhancing neural networks performance in computer vision tasks. The methods that we tested are a first step towards the goal of this promising research field. Optimizing and automatizing the pipeline to produce high-throughput data of 3D samples, would provide the scientific community an easy-to-use computational workflow.

Methods

Human gastruloids
RUES2-GLR hESCs (I. Martyn et al., 2018) have been employed to generate human gastruloids, modifying the protocol developed by Olmsted and Paluh, 2021. 2D hESCs cultured in mTeSR1 (STEMCELL Technologies) are pre-treated for two days prior to dissociation for aggregation, using the N2B27 basal medium (Olmsted and Paluh, 2021) with addition of CHIR 99021 (3 uM) (Tocris Bioscience, 4423) and FGF2 (40 ng/mL) (R&D Systems, 233-FB). Aggregation (Day 0) is performed plating 4 million cells/well in a 6-well plate in N2B27 basal medium with FGF2 (10 ng/mL), HGF (2 ng/mL) (R&D Systems, 294-HG), IGF-1 (2 ng/mL) (R&D Systems, 291-G1) and CHIR 99021 (3uM), on a shaker (75 rpm). We prolonged the CHIR 99021 presence in the medium at Day 1, compared to the initial protocol. At day 4, the medium is replaced with N2B27 basal medium, and from this point on the medium is changed every 3-5 days. For this study, the first round of aggregation has been used for gastruloids at day 1, day 3 and day 4, and the second round of aggregation for gastruloids at day 7, day 10 and day 13.

Immunofluorescence
Gastruloids were fixed at 4°C for 2h using 10% Neutral Formalin solution (HT5011-1CS) by rocking. Samples were then washed 3x with PBS R.T. and permeabilized with 0.2% Triton-X100 in PBS at 4°C by rocking. Blocking was done with 1% BSA-PBST 4°C overnight by rocking. Primary goat anti-FOXA2 antibodies (5 ug/mL) (R&D Systems, AF2400) were incubated at 4°C for 48h-72h by rocking. Secondary antibody, donkey anti-

goat conjugated with Alexa Fluor 647, are diluted 1:1000 in the blocking buffer and incubated overnight at 4°C by rocking. Samples are then washed 2x with blocking buffer and 2x with PBST. Gastruloids are equilibrated with 0.02M phosphate buffer Triton-X100 0.2% (PB-T). Post-fixation was done with 10% Neutral Formalin solution for 20 minutes at 4°C. For a better resolution, gastruloids were cleared using 88% Histodenz solution (D2158-100G) in 0.02M PB-T for 24h-48h at 4°C. Finally, gastruloids (n = 23) were mounted on a coverslip and imaged on a Leica SP8 confocal microscope (Z-plane: 1 um/slice).

Segmentation

To perform nuclear segmentation, we processed two channels independently, FOXA2 and SOX17, using Cellpose, a Convolutional Neural Network implemented in the Google Colab (https://colab.research.google.com/github/MouseLand/cellpose/blob/master/notebooks/Cellpose_2D_v0_1.ipynb). Hyperparameters used are cytoplasmic model, cell diameter = 45, flow threshold = 1 and cell probability threshold = 0. The flow threshold is the maximum allowed error for the flow of each mask (default = 0.4). The cell probability threshold is the probability that an object is a cell (default = 0). Applying the masks produced by Cellpose, we measured mean intensity values of each nucleus segmented on FOXA2 and SOX17 channels in Fiji.

Cluster definition and aspect ratio measurement

We manually drew two lines on all scatterplots where the mean intensities of both markers are visualized, to define three clusters: FOXA2$^+$, FOXA2$^+$/SOX17$^+$ and SOX17$^+$. Ellipses are fitted to each cell in Fiji. The aspect ratio is computed as ratio between major and minor axes. The Mann-Whitney test has been applied using the wilcox.test function (paired = FALSE) in R, to evaluate whether the aspect ratio distributions of the three clusters defined are significantly different.

Cellular alignment

We calculated the pairwise Euclidean distance and pairwise angle difference of segmented nuclei with custom functions in R. When computing the distance, we considered cells centers of body mass (centroids). The angle measured in Fiji for every segmented nucleus corresponds to the major axis inclination of the ellipse fitted to the cells. Considering that samples are fixed, and it is not possible to infer information about directionality, the angles with a difference > 90° are scaled by 180°. The data are processed in R, grouping nuclei by Z-slices and replicates.

Once the pairwise distance and angle difference for every Z-plane are measured, a heatmap is generated to visualize the joint distribution of the two variables, distance and angle difference. Next, we generated a randomized dataset to visualize a random heatmap: pairwise distances are authentic, but a random angle is assigned to every nucleus, generating random counts in the bins. To produce a ratio heatmap between the authentic dataset and the randomized, we divided the occurrences for each bin, and we

plotted the $\log_2$ of the count ratio. Testing elongated SOX17$^+$ nuclei (aspect ratio greater than 1.5), we used as negative control SOX17$^+$ nuclei with aspect ratio lower than 1.5.
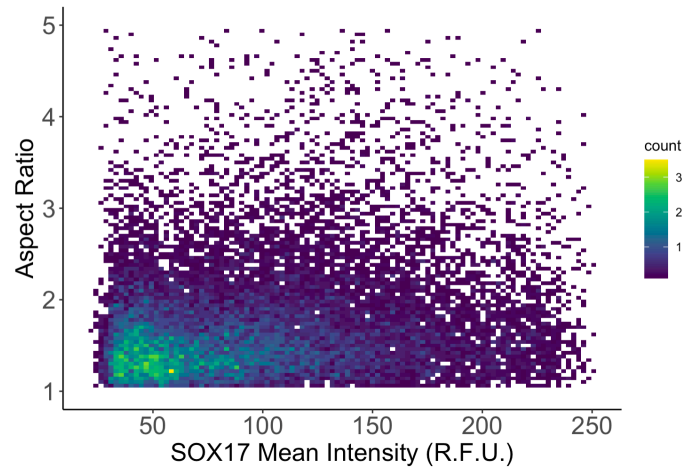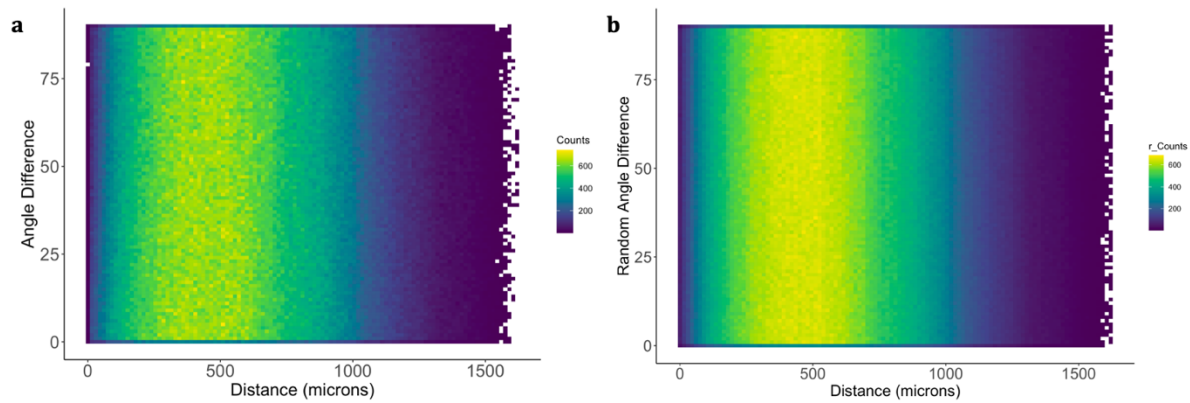
Supplementary Figures
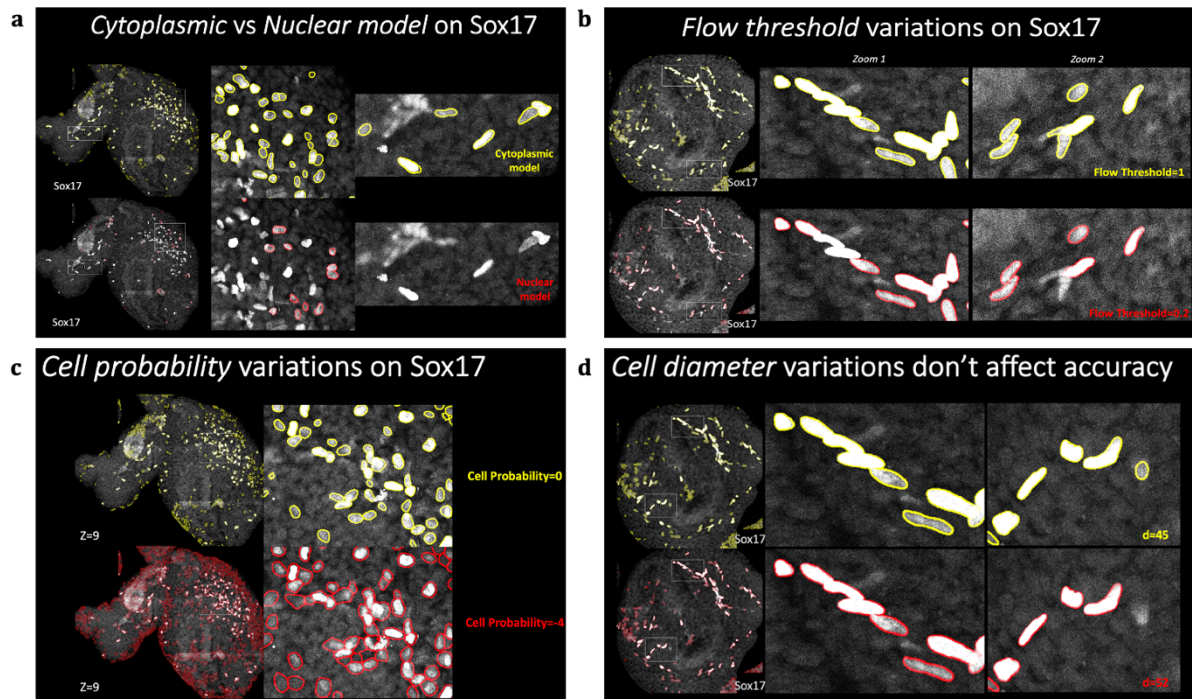
Supplementary Fig. 1: Cellpose hyperparameter adjustment enable accurate SOX17 segmentation. a) Cytoplasmic model (yellow) includes more true positive nuclei than the nuclear model (red). b) Flow threshold = 1 (yellow) is more accurate when segmenting SOX17 nuclei, when compared to flow threshold = 0.2 (red). c) Variations of cell probability from default value (0, yellow) segment a distorted nuclear area; as an example, cell probability = -4. d) Cell diameter variations do not affect segmentation accuracy. In yellow diameter = 45, in red diameter = 52.
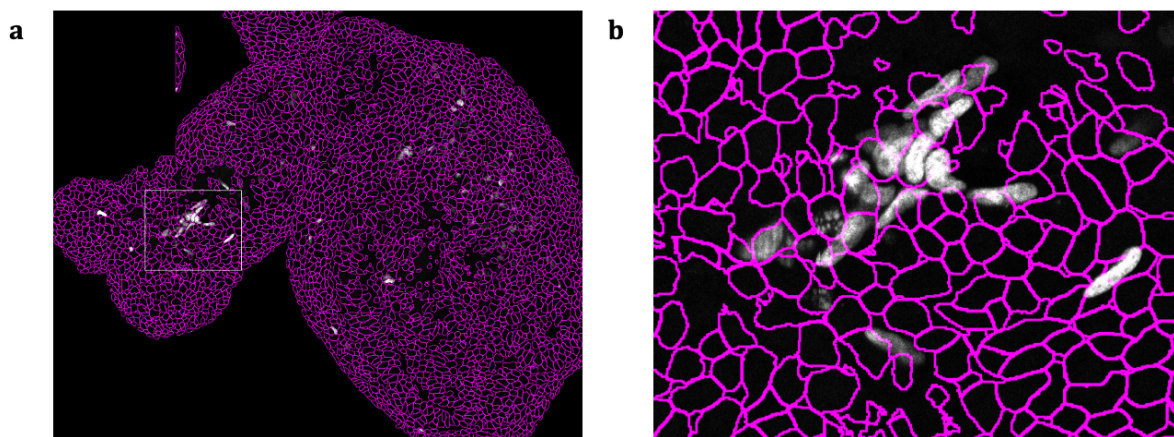
Supplementary Fig. 2: DAPI masks wrongly annotate SOX17 nuclear shape. a) Single Z of a RUES2-GLR human gastruloid. SOX17 channel represented in gray, DAPI masks illustrated in magenta. b) Zoom-in.

Supplementary Fig. 3: No correlation observed between SOX17 mean intensity and aspect ratio. The heatmap clusters all single SOX17+ nuclei in bidimensional bins. On the x-axis the mean intensity of SOX17, on the y-axis the aspect ratio.

Supplementary Fig. 4: Generation of the ratio heatmap in SOX17 cluster of day 13 PA human gastruloid. a) Heatmap of the original elongated dataset. On the x-axis the pairwise Euclidean distance, on the y-axis the pairwise angle difference. Each occurrence illustrates paired measurements of two nuclei. b) Heatmap of the randomized elongated dataset. On the x-axis the pairwise Euclidean distance, on the y-axis the pairwise angle difference. Each occurrence illustrates paired measurements of two nuclei.

The heatmap in Fig. 5d is the result of the ratio between heatmap of the original dataset (a) and the heatmap of the randomized dataset (b).
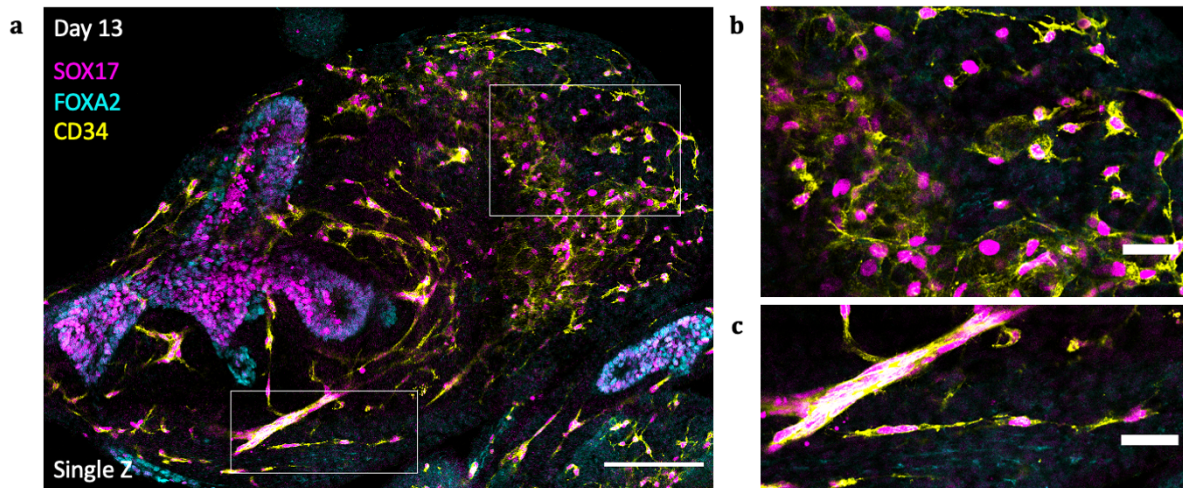
Supplementary Fig. 5: Elongated SOX17⁺ nuclei are disposed as single file compared to rounded SOX17⁺ nuclei. a) Single Z day 13 RUES2-GLR human gastruloid expresses SOX17, FOXA2 and CD34. Scale bar, 200 um. b) Zoom-in: rounded SOX17$^+$ nuclei. Scale bar, 50 um. c) Zoom-in: elongated SOX17$^+$ nuclei. Scale bar, 50 um.

Acknowledgements

References

Abdulateef, S., & Salman, M. (2021). A Comprehensive Review of Image Segmentation Techniques. *Iraqi Journal for Electrical and Electronic Engineering*, *17*(2), 166–175. https://doi.org/10.37917/ijeee.17.2.18

Alexander, A., Jiang, A., Ferreira, C., & Zurkiya, D. (2020). An Intelligent Future for Medical Imaging: A Market Outlook on Artificial Intelligence for Medical Imaging. *Journal of the American College of Radiology*, *17*(1), 165–170. https://doi.org/10.1016/j.jacr.2019.07.019

Berg, S., Kutra, D., Kroeger, T., Straehle, C. N., Kausler, B. X., Haubold, C., Schiegg, M., Ales, J., Beier, T., Rudy, M., Eren, K., Cervantes, J. I., Xu, B., Beuttenmueller, F., Wolny, A., Zhang, C., Koethe, U., Hamprecht, F. A., & Kreshuk, A. (2019). Ilastik: Interactive Machine Learning for (Bio)Image Analysis. *Nature Methods*, *16*(12), 1226–1232. https://doi.org/10.1038/s41592-019-0582-9

Burtscher, I., & Lickert, H. (2009). Foxa2 regulates polarity and epithelialization in the endoderm germ layer of the mouse embryo. *Development*, *136*(6), 1029–1038. https://doi.org/10.1242/dev.028415

Deglincerti, A., Etoc, F., Guerra, M. C., Martyn, I., Ruzo, A., Simunovic, M., Yoney, A., Brivanlou, A. H., Warmflash, A., & Embryology, M. (2018). *HHS Public Access*. *11*(11), 2223–2232. https://doi.org/10.1038/nprot.2016.131.Self-organization

Fu, J., Warmflash, A., & Lutolf, M. P. (2021). Stem-cell-based embryo models for fundamental research and translation. *Nature Materials*, *20*(2), 132–144. https://doi.org/10.1038/s41563-020-00829-9

Ghimire, S., Mantziou, V., Moris, N., & Martinez Arias, A. (2021). Human gastrulation: The embryo and its models. *Developmental Biology*, *474*(January), 100–108. https://doi.org/10.1016/j.ydbio.2021.01.006

Habibi Aghdam, H., Jahani Heravi, E., & AG, S. I. P. (2018). *Guide to Convolutional Neural Networks A Practical Application to Traffic-Sign Detection and Classification*.

Jodele. (2016). 乳鼠心肌提取 HHS Public Access. *Physiology & Behavior*, *176*(1), 100–106. https://doi.org/10.1016/j.semcdb.2016.08.015.Molecular

Khatak, A. (2018). A review on various filtering techniques in image processing. *National Journal of Multidisciplinary Research and Development*, *3*(1), 1350–1355.

Lin, G. G., Finger, E., Gutierrez-Ramos, J. C. (1995). Expression of CD34 in endothelial cells, hematopoietic progenitors and nervous cells in fetal and adult mouse tissues. *European journal of immunology 25(6).*

M. Christopher, A. M. L. S. (2016). 乳鼠心肌提取 HHS Public Access. *Physiology & Behavior*, *176*(1), 100–106. https://doi.org/10.1038/nmeth.3016.A

Minn, K. T., Fu, Y. C., He, S., Dietmann, S., George, S. C., Anastasio, M. A., Morris, S. A., & Solnica-Krezel, L. (2020). High-resolution transcriptional and morphogenetic profiling of cells from micropatterned human esc gastruloid cultures. *ELife*, *9*, 1–34. https://doi.org/10.7554/eLife.59445

Moris, N., Anlas, K., van den Brink, S. C., Alemany, A., Schröder, J., Ghimire, S., Balayo, T., van Oudenaarden, A., & Martinez Arias, A. (2020). An in vitro model of early anteroposterior organization during human development. *Nature*, *582*(7812), 410–415. https://doi.org/10.1038/s41586-020-2383-9

Nakajima-Takagi, Y., Osawa, M., Oshima, M., Takagi, H., Miyagi, S., Endoh, M., Endo, T. A., Takayama, N., Eto, K., Toyoda, T., Koseki, H., Nakauchi, H., & Iwama, A. (2013). Role of SOX17 in hematopoietic development from human embryonic stem cells. *Blood*, *121*(3), 447–458. https://doi.org/10.1182/blood-2012-05-431403

Norman P Spack Daniel E Shumer, N. J. N. (2017). 乳鼠心肌提取 HHS Public Access. *Physiology & Behavior*, *176*(12), 139–148. https://doi.org/10.1177/0962280214537344.Quantitative

Olmsted, Z. T., & Paluh, J. L. (2021). Co-development of central and peripheral neurons with trunk mesendoderm in human elongating multi-lineage organized gastruloids. *Nature Communications*, *12*(1), 1–19. https://doi.org/10.1038/s41467-021-23294-7

Pusztaszeri, M. P., Seelentag, W., & Bosman, F. T. (2006). Immunohistochemical expression of endothelial markers CD31, CD34, von Willebrand factor, and Fli-1 in normal human tissues. *Journal of Histochemistry and Cytochemistry*, *54*(4), 385–395. https://doi.org/10.1369/jhc.4A6514.2005

Radice, G. L., Rayburn, H., Matsunami, H., Knudsen, K. A., Takeichi, M., & Hynes, R. O. (1997). Developmental defects in mouse embryos lacking N-cadherin. *Developmental Biology*, *181*(1), 64–78. https://doi.org/10.1006/dbio.1996.8443

Reviewer, P., & Reviewer, S. (2010). The Patient Experience in Medical Imaging: A Qualitative Systematic Review (protocol). *JBI Library of Systematic Reviews*, *8*(Supplement), 1–15. https://doi.org/10.11124/jbisrir-2010-853

Robert Cronin Yung Peng, Rose Khavari, N. D. (2017). 乳鼠心肌提取 HHS Public Access. *Physiology & Behavior*, *176*(3), 139–148. https://doi.org/10.1159/000444169.Carotid

Schoenwolf G. C., Larsen, W. J. (2019). *Larsen's Human Embryology*. Philadelphia: Churchill Livingstone/Elsevier.

Shao, Y., Taniguchi, K., Townshend, R. F., Miki, T., Gumucio, D. L., & Fu, J. (2017). A pluripotent stem cell-based model for post-implantation human amniotic sac development. *Nature Communications*, *8*(1), 1–15. https://doi.org/10.1038/s41467-017-00236-w

Sidney, L. E., Branch, M. J., Dunphy, S. E., Dua, H. S., & Hopkinson, A. (2014). Concise review: Evidence for CD34 as a common marker for diverse progenitors. *Stem Cells*, *32*(6), 1380–1389. https://doi.org/10.1002/stem.1661

Soliman, K. (2015). CellProfiler: Novel Automated Image Segmentation Procedure for Super-Resolution Microscopy. *Biological Procedures Online*, *17*(1), 1–7. https://doi.org/10.1186/s12575-015-0023-9

Stringer, C., Wang, T., Michaelos, M., & Pachitariu, M. (2021). Cellpose: a generalist algorithm for cellular segmentation. *Nature Methods*, *18*(1), 100–106. https://doi.org/10.1038/s41592-020-01018-x

Valizadeh, A., & Shariatee, M. (2021). The Progress of Medical Image Semantic Segmentation Methods for Application in COVID-19 Detection. *Computational Intelligence and Neuroscience*, *2021*. https://doi.org/10.1155/2021/7265644

van den Brink, S. C., & van Oudenaarden, A. (2021). 3D gastruloids: a novel frontier in stem cell-based in vitro modeling of mammalian gastrulation. *Trends in Cell Biology*, *31*(9), 747–759. https://doi.org/10.1016/j.tcb.2021.06.007

Weng, W., & Zhu, X. (2021). INet: Convolutional Networks for Biomedical Image Segmentation. *IEEE Access*, *9*, 16591–16603. https://doi.org/10.1109/ACCESS.2021.3053408

Wolf, S., Wan, Y., & McDole, K. (2021). Current approaches to fate mapping and lineage tracing using image data. *Development (Cambridge)*, *148*(18). https://doi.org/10.1242/DEV.198994

Yang, J., Ii, M., Kamei, N., Alev, C., Kwon, S. M., Kawamoto, A., Akimaru, H., Masuda, H., Sawa, Y., & Asahara, T. (2011). CD34+ cells represent highly functional endothelial progenitor cells in murine bone marrow. *PLoS ONE*, *6*(5), 1–14. https://doi.org/10.1371/journal.pone.0020219